Statistical Analysis of Whistler Precursors Upstream of Foreshock Transient Shocks: MMS Observations

Mengmeng Wang, Terry Z. Liu, Hui Zhang, Kaijun Liu, Quanqi Shi, Ruilong Guo, Anmin Tian, Weijie Sun, Xiao-Chen Shen, Siyuan Wu, et al.

Geophysical Research Letters

RESEARCH LETTER
10.1029/2023GL105617

Statistical Analysis of Whistler Precursors Upstream of Foreshock Transient Shocks: MMS Observations

Mengmeng Wang[1,2], Terry Z. Liu[3], Hui Zhang[1], Kaijun Liu[2], Quanqi Shi[1], Ruilong Guo[1], Anmin Tian[1], Weijie Sun[4], Xiao-Chen Shen[5], Siyuan Wu[2,6], Alexander W. Degeling[1], Yan Wang[2], Shi-Chen Bai[1,7], Zhonghua Yao[8], Wenya Li[9], Shuai Zhang[2], Timo Pitkänen[1,10], Shutao Yao[1], Ji Liu[11], Kun Cheng[2], Xiao Ma[1], and Yuqi Liu[2]

[1]Shandong Provincial Key Laboratory of Optical Astronomy and Solar-Terrestrial Environment, Institute of Space Sciences, Shandong University, Weihai, China, [2]Department of Earth and Space Sciences, Southern University of Science and Technology, Shenzhen, China, [3]Department of Earth, Planetary, and Space Sciences, University of California, Los Angeles, Los Angeles, CA, USA, [4]Space Sciences Laboratory, University of California, Berkeley, Berkeley, CA, USA, [5]Center for Space Physics, Boston University, Boston, MA, USA, [6]LESIA, Observatoire de Paris, CNRS, Université PSL, Sorbonne Université, Université Paris Cité, CNRS, Meudon, France, [7]School of Mathematics and Statistics, Shandong University, Weihai, China, [8]Department of Earth Sciences, The University of Hong Kong, Hong Kong, China, [9]State Key Laboratory of Space Weather, National Space Science Center, Chinese Academy of Sciences, Beijing, China, [10]Department of Physics, Umeå University, Umeå, Sweden, [11]Department of Physics, University of Alberta, Edmonton, AB, Canada

Key Points:

- Precursor waves upstream of foreshock transient shocks are found to follow the whistler wave dispersion relation in the plasma rest frame
- The occurrence of whistler precursors is independent of the Alfvén Mach numbers and normal angles of the foreshock transient shocks
- The observed wave characteristics are consistent with that the precursors are generated through the dispersive radiation mechanism

Correspondence to:
K. Liu and Q. Shi,
liukj@sustech.edu.cn;
sqq@sdu.edu.cn

Citation:
Wang, M., Liu, T. Z., Zhang, H., Liu, K., Shi, Q., Guo, R., et al. (2024). Statistical analysis of whistler precursors upstream of foreshock transient shocks: MMS observations. *Geophysical Research Letters*, *51*, e2023GL105617. https://doi.org/10.1029/2023GL105617

Received 1 AUG 2023
Accepted 29 FEB 2024

Abstract Using the high-time-resolution data from the Magnetospheric Multiscale mission, precursor waves upstream of foreshock transient (FT) shocks are statistically investigated using the four-spacecraft timing method. The wave frequencies and wave vectors determined in the plasma rest frame (PRF) are shown to follow the cold plasma dispersion relation for whistler waves. Combining with the feature of the right-hand polarization in the PRF, the precursors are identified as whistler-mode waves around the lower hybrid frequency. The occurrence of whistler precursors is independent of the Alfvén Mach number and the FT shock normal angle. More importantly, all the whistler precursors have group velocities pointing upstream in the shock frame, suggesting the dispersive radiation to be a possible generation mechanism. The study improves the understanding of not only the whistler precursors but also the overall FT shock dynamics.

Plain Language Summary The characteristics of the precursor waves upstream of foreshock transient (FT) shocks are determined in the plasma rest frame using the multi-point measurements from the Magnetospheric Multiscale mission with appropriate separation scales. The statistical results demonstrate for the first time that the precursors upstream of FT shocks are lower hybrid frequency whistler-mode waves. The presence or absence of large amplitude whistler precursors does not depend on the FT shock normal angle and the Alfvén Mach number. These results have important implications on the nature of the whistler precursors and the dynamics of the FT shocks.

1. Introduction

Whistler precursors were widely observed within or upstream of planetary bow shocks (Brain et al., 2002; Fairfield & Behannon, 1976; Lalti et al., 2022; Orlowski & Russell, 1991; Orlowski et al., 1992; Russell, 2007; Smith et al., 1991; Sulaiman et al., 2017; Y. Wang et al., 2023), interplanetary shocks (Wilson et al., 2017, 2021), and near lunar crustal magnetic sources (Halekas et al., 2006; Harada & Halekas, 2016). They are believed to be an essential part of collisionless shocks (Balogh & Treumann, 2013; Kennel et al., 1985; Wilson, 2016) and may be driven by plasma instabilities (Matsukiyo & Scholer, 2006; Scudder et al., 1986; Wilson et al., 2012) or radiated from shock ramps (Balikhin et al., 1997; Krasnoselskikh et al., 2002; Sundkvist et al., 2012). Previous theories and simulations suggest that whistler precursors lie on the same dispersion relation branch as fast magnetosonic/whistler waves. These waves are expected to be right-hand polarized electromagnetic waves in the frequency range of $\omega_{ci} \ll \omega \ll \omega_{ce}$, where ω_{ci}, ω, and ω_{ce} are the proton cyclotron, wave, and electron cyclotron (angular) frequencies, respectively. Whistler precursors have various effects in shock dynamics, such as modifying shock transitions (Scholer & Burgess, 2007; Scholer et al., 2003), transferring energy between ions and electrons (Hull et al., 2020; Muschietti & Lembège, 2017), and redistributing electrons to drive instabilities (Z. Y. Liu et al., 2021; Yao et al., 2021). They have also been shown to accelerate, scatter, and/or heat electrons (Hull

et al., 2012, 2020; Oka et al., 2019; Wilson et al., 2012). In addition, whistler precursors have been observed upstream of the foreshock transient (FT) shocks in the Earth's foreshock (e.g., Turner et al., 2020, 2021). The foreshock is filled with back-streaming ions from the Earth's bow shock (Eastwood, Balogh, et al., 2005; Eastwood, Lucek, et al., 2005). Interactions between the back-streaming ions and a solar wind (SW) discontinuity can generate an FT with a core of low magnetic field magnitude and plasma density, which is bounded by compressional boundaries (Lin, 1997; Omidi et al., 2010; Schwartz et al., 1985; Turner et al., 2013; Zhang et al., 2022). If the expansion of plasma in an FT core is supermagnetosonic, the upstream compressional boundary can steepen into a secondary shock, that is, an FT shock (An et al., 2020; T. Z. Liu et al., 2020).

Whistler precursors are observed by spacecraft flying through local plasmas. The corresponding Doppler shift obscures the true identity of these waves and makes it challenging to unequivocally determine their properties in the plasma rest frame (PRF) from observations. Due to the spatial-temporal ambiguity, wavelengths (and the corresponding phase speeds, etc.) cannot be reliably calculated using measurements from a single satellite without making assumptions (Sonnerup & Scheible, 1998). As for observations from dual spacecraft, wavelengths can be obtained only when the wave propagation directions (represented as $\hat{\boldsymbol{k}}$) have been determined (e.g., by the minimum variance analysis) in some special conditions (Eastwood, Balogh, et al., 2005; Eastwood, Lucek, et al., 2005; Mellott & Greenstadt, 1984). Measurements from four spacecraft with appropriate separations are needed in order to accurately calculate the wavelengths (Krasnoselskikh et al., 2013; Mazelle et al., 2010). Thanks to the Magnetospheric Multiscale (MMS) constellation mission with small inter-spacecraft separations of tens of kilometers, the four-spacecraft timing method has been successfully applied to determine the wave vectors and phase speeds of electromagnetic waves around the lower hybrid frequency (Hull et al., 2020; Lalti et al., 2022). With unambiguous wave vectors and SW velocities, the corresponding Doppler shifts can be corrected so that the wave frequencies in the PRF can be determined. Finally, the wave dispersion relation as well as their polarization properties in the PRF can be obtained to unequivocally reveal the wave identity.

The properties of precursor waves (PWs) upstream of FT shocks are crucial to confirm their possible generation mechanisms. Up to now, it is uncertain whether the properties of FT shock precursors are different from the ones observed at planetary bow shocks and interplanetary shocks. The upstream plasma velocities for FT shocks are much smaller than that of planetary bow shocks (T. Z. Liu et al., 2016; Turner et al., 2020, 2021). This results in smaller Mach numbers for FT shocks. It is still unclear in what Mach number and shock normal angle ranges (the angle between the shock normal and the upstream magnetic field) the precursors tend to occur for FT shocks. A statistical study of FT shock precursors and their relationship with the FT shock parameters is needed to gain insights on the above unsettled questions. The present study surveys the MMS observations to statistically examine the PWs observed upstream of FT shocks. The four-spacecraft timing method is employed to extract the wave phase speeds and the wave vectors, etc., in the PRF. The correlation between the precursor occurrence and the FT shock parameters is also explored. The rest of the paper is organized as follows. Section 2 describes the spacecraft data used and how the FT shock precursor events have been selected. Wave properties in both the spacecraft frame (SCF) and the PRF are analyzed in Section 3. Section 4 presents the relationship between the precursors and their corresponding FT shock parameters. Section 5 discusses possible generation mechanisms of the PWs upstream of FT shocks. Finally, the conclusions are summarized in Section 6.

2. Data and Event Selection

The high-time-resolution data from the MMS mission (Burch et al., 2016) were used to conduct this study. The ion and electron data are from the fast plasma investigation (FPI) instrument (Pollock et al., 2016) with temporal resolutions of 0.15 and 0.03 s, respectively. Magnetic field data with a sampling rate of 128 Hz are from the fluxgate magnetometer (FGM) (Russell et al., 2016). The AC magnetic field data with a sampling rate of 8,192 Hz are from the search-coil magnetometer instrument (SCM) (Le Contel et al., 2016). The Geocentric Solar Ecliptic (GSE) coordinate system is used throughout this study.

Initially, the selection criteria of FTs summarized by Vu et al. (2022) were used and 207 FTs were selected using MMS data from 2015 to 2022. Whether these FTs are foreshock bubbles or hot flow anomalies is irrelevant for the purposes of this study, hence we do not identify or differentiate them. Next, FT shocks associated with the 207 selected FTs were identified following similar criteria as in Davis et al. (2021) that include the ratios of downstream to upstream magnetic field (B_{down}/B_{up}) and ion density (N_{down}/N_{up}), the change in the velocity

magnitude ($|\Delta V| = |V_{\rm down} - V_{\rm up}|$), and the presence of a compressional sheath. In particular, if the outer discontinuity on the trailing edge of an FT satisfies

$$B_{\rm down}/B_{\rm up} \geq 1.5,$$

$$N_{\rm down}/N_{\rm up} \geq 1.5,$$

$$|\Delta V| = |V_{\rm down} - V_{\rm up}| \geq 20 \text{ km s},^{-1}$$

and is accompanied by a compressional sheath, it is identified as an FT shock. The downstream-to-upstream ion temperature ratio is not considered because the SW ion temperatures measured are unreliable due to the insufficient resolving capacity for the narrow distribution of SW ions (e.g., see Wilson et al., 2022). The above identification criteria yield 46 FT shocks. The fluctuations on the ramp or foot of these FT shocks are then recognized as PWs if the ratio of the maximum peak-to-peak wave amplitude to the ambient magnetic field at the start of each event, $\delta B/B_0$, is larger than 0.01. Out of the identified 46 FT shocks, 36 of them exhibit PWs.

An example event is shown in Figure 1. Around 04:19 UT on 10 December 2018, MMS observed an FT as shown in Figures 1a–1d. The FT is characterized by a core of low magnetic field magnitude and plasma density surrounded by compressional boundaries. It has a shock on its trailing boundary at 04:20:02 UT. Figures 1a and 1b display the complex FT shock including large-amplitude PWs (Turner et al., 2020; Wilson, 2016). The characteristics of this FT shock and the associated fluctuations meet the selection criteria described above, therefore, this FT shock case with PWs is included in our database.

3. Properties of PWs

In order to obtain the properties of the FT shock PWs in the PRF, the cross-correlation analysis was performed on measurements from the four MMS spacecraft (Hull et al., 2020; S. Wang et al., 2020). The MMS magnetic field measurements during intervals of interest were first band-pass filtered in the frequency range of 0.5–6 Hz, which eliminates the 3-s ultralow frequency signals and covers the spectral peaks of the PWs. In this study, an interval would be rejected if the cross-correlation coefficient of any spacecraft pair is less than 0.8, because the relevant magnetic field time series are then not adequately correlated. Note that the analysis is for the Y component of the wave magnetic field ($\boldsymbol{B}_w$) only, because it has the largest amplitude (and therefore, the best signal-to-noise ratio) among the three $\boldsymbol{B}_w$ components for most cases. Together with the spacecraft separation information, the time lags obtained from the cross-correlation analysis served as inputs for calculating $\hat{\boldsymbol{k}}$ and phase speeds in the SCF ($v_{\rm ph}^{\rm scf}$). These calculations were performed using the four-spacecraft timing analysis method, as described in previous studies (Schwartz, 1998; Shi et al., 2019). Finally, a reference frame transformation was applied based on the SW velocity ($\boldsymbol{v}_{\rm sw}$) to calculate the wave phase speeds in the PRF

$$v_{\rm ph}^{\rm prf} = v_{\rm ph}^{\rm scf} - \boldsymbol{v}_{\rm sw} \cdot \hat{\boldsymbol{k}}. \quad (1)$$

The present study relies on the level-2 velocity moments measured by the FPI instrument to get $\boldsymbol{v}_{\rm sw}$. Although the level-2 data contain the contribution of possible back-streaming ions (Wilson et al., 2014) and may cause $\boldsymbol{v}_{\rm sw}$ to deviate from its exact value, the careful removal of the back-streaming ion contamination in $\boldsymbol{v}_{\rm sw}$ is challenging.

In Figures 1e and 1f, the PWs upstream of the FT shock are evident. Figure 1g further shows the spectrogram of the magnetic field. The PWs shown in Figure 1f were found to have a $v_{\rm ph}^{\rm scf}$ of 353 km/s and $\hat{\boldsymbol{k}} = [-1, -0.04, 0.05]$. Given that the background magnetic field during the interval is [2.7, −0.9, 2.6] nT, the wave normal angle ($\theta_{\rm kB}$) is 48°. In addition, the corresponding phase speed in the PRF is −268 km/s, representing a sunward-propagating wave. Finally, the wavelength is frame-independent and can be obtained directly from measurements in the SCF: $\lambda \equiv V_{\rm ph}^{\rm scf}/f_{\rm scf} = 88$ km, where the frequency in the SCF ($f_{\rm scf}$) is 4.0 Hz. Thus, the PRF frequency $f_{\rm prf} = f_{\rm scf} - \boldsymbol{v}_{\rm sw} \cdot \frac{\hat{\boldsymbol{k}}}{\lambda} = -3.0$Hz. Note that the wave frequency becomes negative in the PRF from being positive in the SCF, because the wave phase velocity is less than the $\boldsymbol{v}_{\rm sw}$ along the wave vector. The sign change of the wave frequency indicates that the wave propagating sunward in the PRF is convected earthward by the SW flow and the wave polarization reverses between the PRF and the SCF.

10.1029/2023GL105617

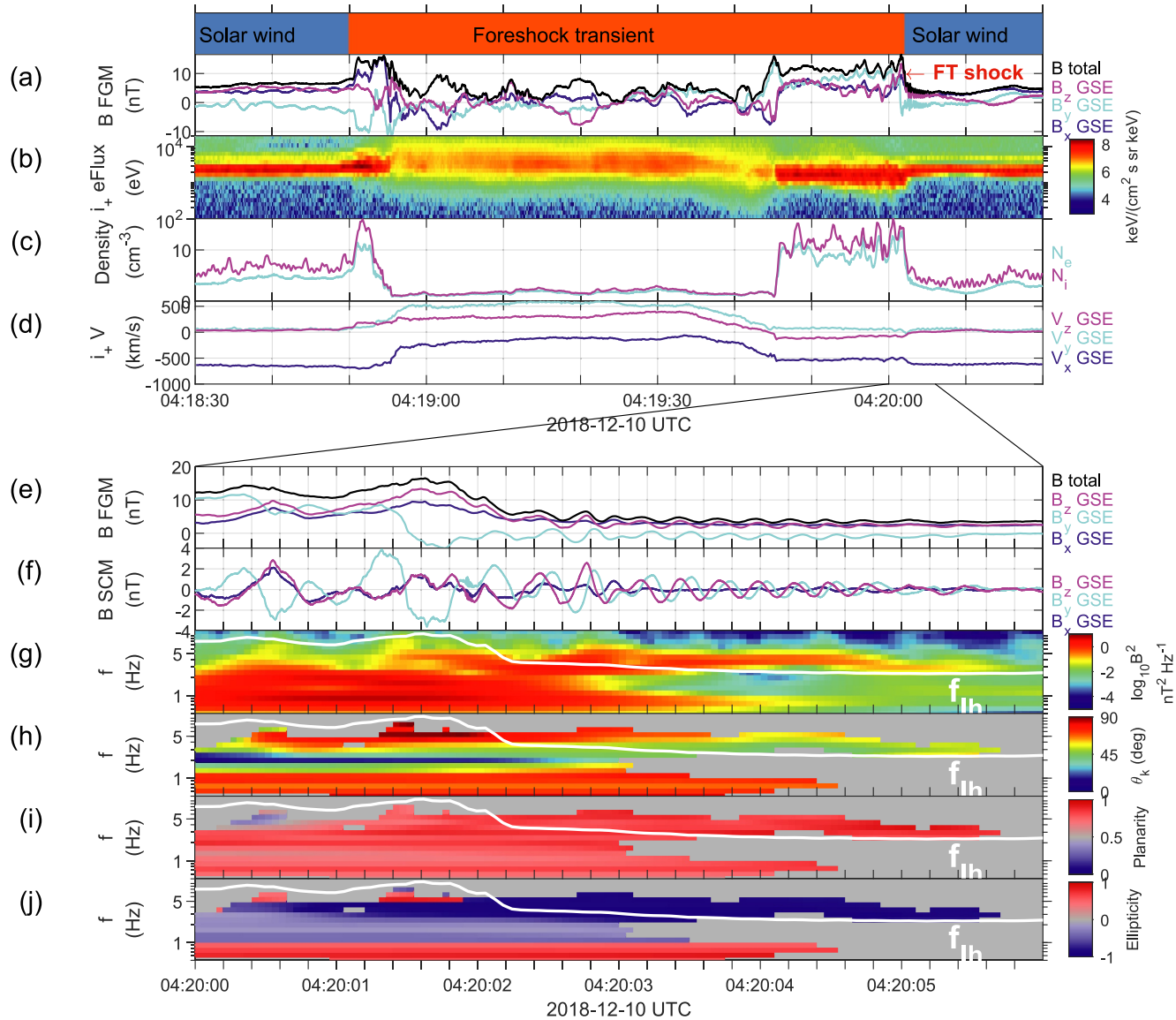

Figure 1. Overview of an FT with PWs at its upstream shock observed by MMS1. (a) Magnetic field components in the GSE coordinates (*X*, *Y*, and *Z* in blue, cyan, and magenta, respectively) and total magnitude (black) from the FGM instrument. (b) Ion omni-directional differential energy flux. (c) Ion (magenta) and electron (cyan) number densities. (d) Ion velocity components in the GSE coordinates (*X*, *Y*, and *Z* in blue, cyan, and magenta, respectively). Panels (e) and (f) are the zoom-in of the FT shock showing the three magnetic field components in the GSE coordinates from the FGM and SCM instruments, respectively. The black curve in panel (e) represents the total magnetic field magnitude as in (a). (g) Spectrogram of the wave magnetic field from the SCM instrument. (h–j) θ_{kB}, planarity and ellipticity determined using the SVD method. In (g)–(j), the white curve indicates the local lower hybrid frequency. Note that the bins corresponding to the waves of power spectrum density below 3×10^{-2} nT^2/Hz in (g) have been removed in (h)–(j) to highlight the results of strong waves.

Since the timing method involves the assumption that $\hat{\boldsymbol{k}}$ remains constant regardless of frequency or that the waves are narrow-band, the singular value decomposition (SVD) method (Santolík et al., 2003) has also been used to determine $\hat{\boldsymbol{k}}$ for cross validation. The SVD method can give $\hat{\boldsymbol{k}}$, planarity, and ellipticity at different frequencies and different times under the plane wave assumption. For the waves shown in Figure 1f, Figures 1h–1j display the θ_{kB}s, planarity, and ellipticity calculated using the SVD method. The θ_{kB}s of the PWs are around 50°, and their power-weighted average gives a θ_{kB} of 54°, consistent with the $\hat{\boldsymbol{k}}$ determined by the timing method. In addition, Figure 1i shows that the planarity of the PWs is close to 1, suggesting plane waves. Figure 1j shows that the ellipticity is close to −1, indicating left-hand, circularly polarized waves (in the SCF). However, as discussed above, the waves are right-hand polarized in the PRF after the large Doppler shift.

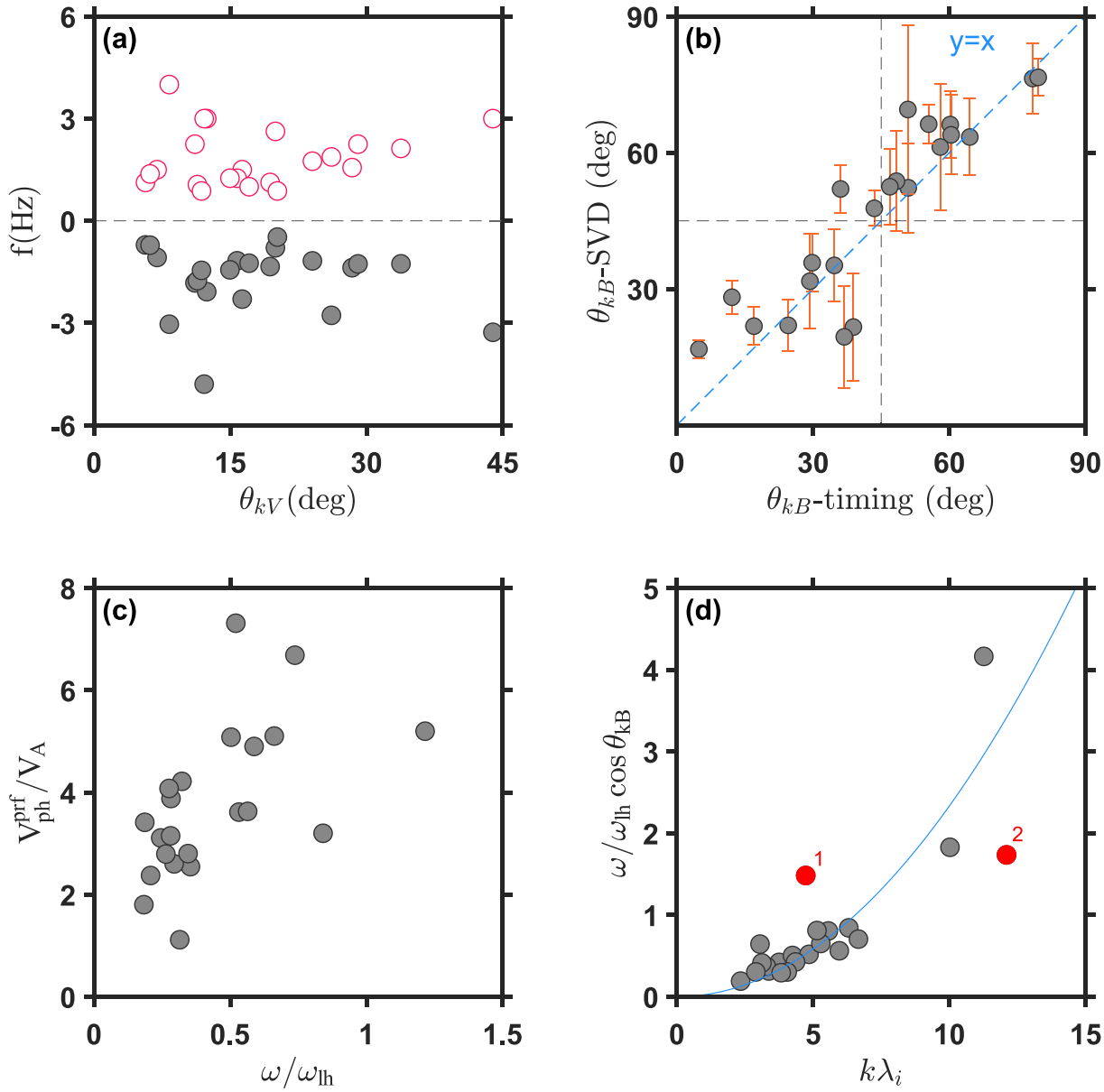

Figure 2. Properties of the 22 FT shock precursor-wave events analyzed using the timing method: (a) the distribution of wave frequencies in the SCF (red circles) and the PRF (gray dots) against θ_{kV}, (b) comparison of θ_{kB}s determined by the SVD and timing methods, (c) distribution of phase speeds (normalized by the local V_A) against frequencies (normalized by ω_{lh}) in the PRF, (d) distribution of frequencies (normalized by $\omega_{lh}\cos\theta_{kB}$) in the PRF against wavenumbers (normalized to the λ_i). The vertical orange bars in (b) denote uncertainties of the θ_{kB}s from the SVD method. The blue line in (d) represents the cold plasma whistler dispersion relation of Equation 4. The two events far off the dispersion relation curve are highlighted in red and explained in the text.

Among the 36 FT shock precursors found, 22 events have cross-correlation coefficients greater than 0.8 in the $\boldsymbol{B}_w$ data. Applying the four-spacecraft timing analysis to the 22 precursors, their frequencies, wave vectors, phase speeds, and polarizations were obtained. Figure 2a displays the distribution of their frequencies in the SCF and the PRF against θ_{kV}, the angle between the wave vector and the background SW velocity direction. The θ_{kV} values are small (<45°), implying strong Doppler shifts between the SCF and the plasma rest (solar wind) frame (Fairfield, 1974; Russell, 2007). For all the PWs analyzed here, their frequencies have different signs in the two reference frames. They are left-handed in the SCF but have a right-hand polarization in the PRF due to the strong Doppler shifts.

The θ_{kB}s of all the 22 precursors from the timing analysis as well as the SVD method are compared in Figure 2b. Note that the θ_{kB}s from the SVD method shown here are the power-weighted averages across different

frequencies. The two sets of θ_{kB}s are consistent with each other, demonstrating the good performance of the four-spacecraft timing method in analyzing the PWs around the lower hybrid frequency. Figure 2b also shows that the precursors propagate obliquely with θ_{kB} varying between 5° and 80°.

Figure 2c displays the phase speeds and the frequencies of the 22 events in the PRF. The phase speeds are between 1.1 and 7.3 V_A, and the frequencies vary from 0.2 to 1.2ω_{lh}, where V_A is the local Alfvén speed and ω_{lh} is the lower hybrid frequency. Figure 2d presents the distribution of the frequencies in the PRF against the wavenumbers. The frequencies are normalized by $\omega_{lh}\cos\theta_{kB}$, and the wavenumbers are normalized to the proton inertial length ($\lambda_i = c/\omega_{pi}$, where c is the light speed and ω_{pi} represents the proton plasma frequency). Owing to the larger measurement uncertainty in the ion density within the SW, the calculation of λ_i uses the local electron density measured by the FPI instrument, assuming quasi-neutrality. As elucidated by Wilson et al. (2022), both the ion and electron densities from the FPI instrument can be underestimated. However, this should not significantly affect the inertial length calculated because it is inversely proportional to the square root of the plasma density. The cold plasma dispersion relation for whistler waves in the frequency range of $\omega_{ci} \ll \omega \ll \omega_{ce}$ can be simplified to (Stringer, 1963; Verkhoglyadova et al., 2010):

$$\frac{\omega}{\omega_{ce}} = \frac{k^2\lambda_e^2 \cos\theta_{kB}}{1 + k^2\lambda_e^2}, \tag{2}$$

where $\lambda_e = c/\omega_{pe}$ is the electron inertial length. Since $k\lambda_e \ll 1$ as shown in Figure 2d, Equation 2 can be further simplified to

$$\frac{\omega}{\omega_{ce}} = k^2\lambda_e^2 \cos\theta_{kB}. \tag{3}$$

Finally, when the frequency and wavenumber are normalized as in Figure 2d, one gets

$$\tilde{\omega} = \sqrt{\frac{m_e}{m_p}}\tilde{k}^2. \tag{4}$$

Here $\tilde{\omega} = \frac{\omega}{\omega_{lh}\cos\theta_{kB}}$, $\tilde{k} = k\lambda_i$, and m_p and m_e are the proton mass and electron mass, respectively. Equation 4 yields the blue dashed curve shown in Figure 2d. The observed PWs nicely follow the blue curve except for two cases highlighted in red. The case labeled as "1" was observed around 14:41 UT on 1 December 2017, and the wave properties are affected by the significant reflected ions from its corresponding FT shock. The precursor case labeled as "2" was observed around 20:27 UT on 5 March 2021, whose wavelength is about 37 km, smaller than twice of the spacecraft separation (27 km). Hence, the timing analysis result may have been affected by aliasing (Lalti et al., 2022). Thus, the good agreement of the PWs with the cold plasma whistler dispersion relation clearly demonstrates that the waves are whistler-mode waves.

4. The Relationship Between Whistler Precursors and FT Shock Parameters

To explore the relationship between the whistler precursors and the FT shock parameters, the normal directions and propagation speeds of FT shocks in the SCF were calculated using the timing method. The coplanarity estimate (Equation 10.17 from Schwartz, 1998) was also used to determine the FT shock normal directions ($\hat{\boldsymbol{n}}$). If the difference of the FT $\hat{\boldsymbol{n}}$ given by the two methods were within 30°, the FT shock case is to be further analyzed. Finally, a total of 29 cases were selected out of the 46 FT shocks identified as described in Section 2. The shock normal angle (θ_{Bn}) was calculated for each case using the $\hat{\boldsymbol{n}}$ given by the timing method and the average upstream magnetic field (during an interval of 5–10 s with the least fluctuations). As the FT shocks propagate sunward in the SW flow, their Alfvén Mach numbers (M_A) are calculated from the upstream $\boldsymbol{v}_{sw}$ in the FT shock frame. The relationship between θ_{Bn} and M_A of the 29 cases is given in Figure 3a. The FT shocks are distributed in the M_A range of 2–7 and θ_{Bn} range of 20°–90°. There are 21 quasi-perpendicular ($\theta_{Bn} > 45°$) shocks and 8 quasi-parallel ($\theta_{Bn} < 45°$) shocks. Also, the 29 cases selected all have $\theta_{Bn} > 20°$. The reason is likely that the fronts of shocks with small θ_{Bn} often undergo significant reformation so their normal directions (and speeds) determined by the timing method and the coplanarity estimate are both not reliable and do not agree with each other within 30°.

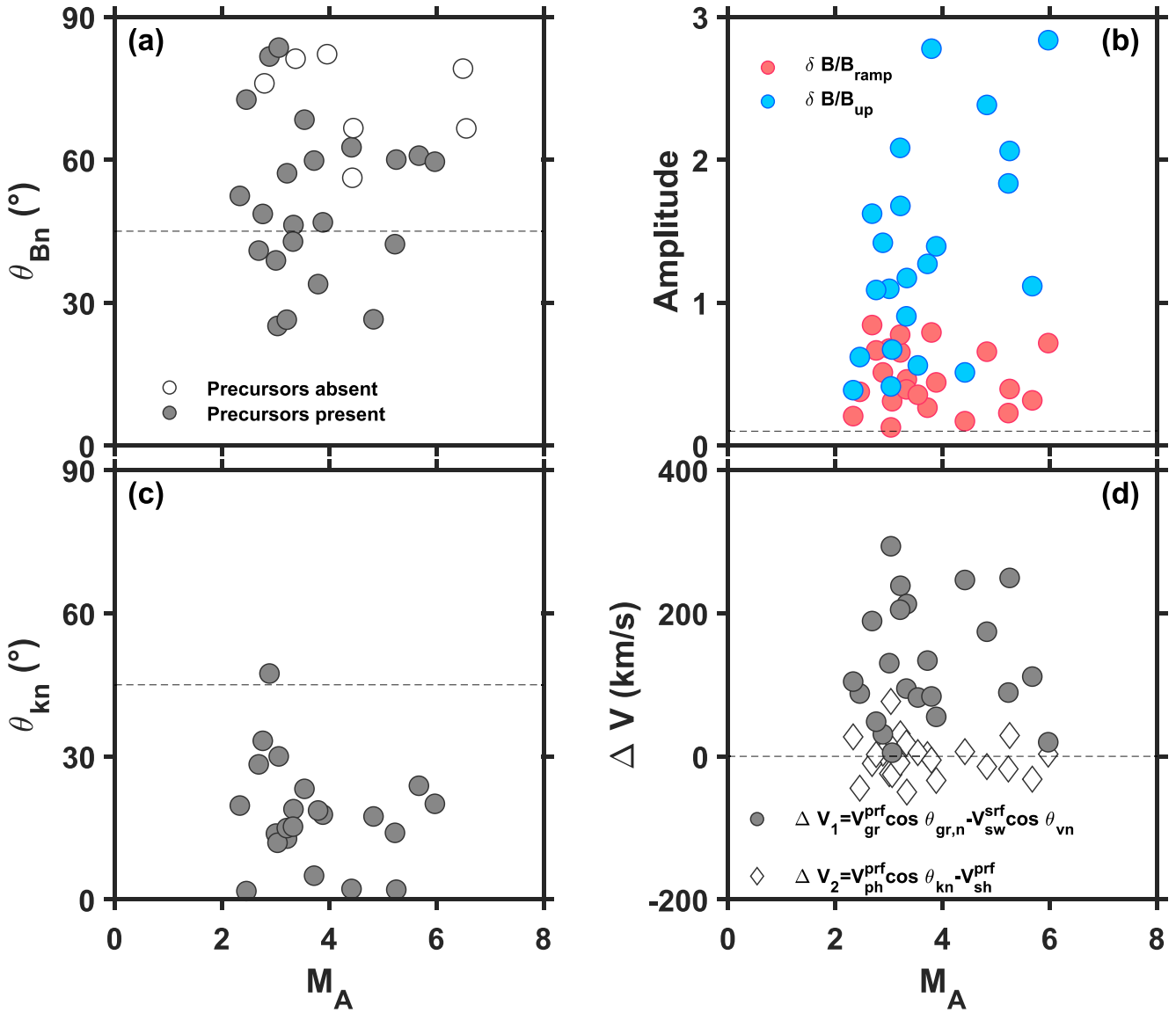

Figure 3. (a) θ_{Bn} against M_A of the 29 FT shock cases selected. The solid dots and empty circles represent the FT shocks with and without whistler precursors, respectively. The horizontal dashed line denotes $\theta_{Bn} = 45°$. Panels (b–d) show the properties of those 22 whistler-precursor cases. (b) The amplitudes of whistler precursors versus M_A of the FT shocks. The red dots denote $\delta B/B_{ramp}$, while the blue dots denote $\delta B/B_{up}$. The horizontal dashed line represents the amplitude of 0.1. (c) θ_{kn} versus M_A. The horizontal dashed line denotes θ_{kn} of 45°. (d) The relative velocities (ΔV) between the whistler precursors and their corresponding FT shocks. The horizontal dashed line denotes $\Delta V = 0$.

Thus, these cases are not included in the analysis. Another possible reason is that nearly all FTs act to generate local quasi-perpendicular regions (e.g., see references in Wilson (2016)).

Among the 29 FT shocks analyzed, 22 cases have whistler precursors. The 8 quasi-parallel shocks analyzed all have precursors, while precursors are observed upstream of 14 out of the 21 quasi-perpendicular shocks (Figure 3a). The relationship between the whistler precursors and the corresponding FT shock parameters is further demonstrated in Figures 3b–3d. Figure 3b displays the whistler-precursor amplitudes versus M_A of the corresponding FT shocks. Here, the red and blue dots represent the precursor amplitudes normalized to the amplitudes of the FT shock ramps (B_{ramp}) and the average background magnetic field magnitudes during the precursor intervals (B_{up}), respectively. The amplitude of a FT shock ramp is defined as the difference between the maximum magnetic magnitude value of the ramp and the average magnetic field magnitude in the upstream region of the FT shock. The whistler precursors have amplitudes comparable to the amplitudes of the

corresponding FT shock ramps ($0.1<\frac{\delta B}{B_{\rm ramp}}<1$). The $\delta B/B_{\rm up}$ values distribute in the range of 0.1–3, and there is a weak trend that $\delta B/B_{\rm up}$ increase with the increase of M_A. The precursor-wave amplitudes are fairly large as the two types of normalized amplitudes both exceed the typical approximate threshold for the separation of linear and nonlinear oscillations (i.e., $\delta B/B \sim 0.1$) (Yoon et al., 2014). Figure 3c shows the angles between $\hat{\boldsymbol{k}}$ and the FT shock normal directions ($\theta_{\rm kn}$) versus M_A. Most whistler precursors propagate at angles smaller than 45° with respect to the FT shock normal directions.

To examine whether the PWs propagate away from or toward the FT shocks, the relative velocities of the precursors to their corresponding FT shocks have been calculated and shown in Figure 3d. For the precursors to propagate upstream of the FT shocks, their group velocities $\left(v_{\rm gr}^{\rm prf}\right)$ need to be greater than the SW velocity $v_{\rm sw}^{\rm srf}$ along the FT shock normal direction, i.e., $\Delta V_1 = v_{\rm gr}^{\rm prf}\cos\theta_{{\rm gr},n} - v_{\rm sw}^{\rm srf}\cos\theta_{\rm vn} > 0$, where $v_{\rm sw}^{\rm srf}$ is the upstream $\boldsymbol{v}_{\rm sw}$ in the FT shock frame, $\theta_{{\rm gr},\,n}$ represents the angle between the group velocity and the FT shock normal direction, and $\theta_{\rm vn}$ is the angle between $\boldsymbol{v}_{\rm sw}$ and the FT shock normal direction. The group velocity in the PRF can be calculated as $\boldsymbol{v}_{\rm gr}^{\rm prf} = \left|\boldsymbol{v}_{\rm ph}^{\rm prf}\right|\left(2\hat{\boldsymbol{k}} - \tan\theta_{\rm kB}\hat{\boldsymbol{\theta}}\right)$ from Equation 4, where $\hat{\boldsymbol{\theta}}$ stands for the direction perpendicular to $\hat{\boldsymbol{k}}$ in the plane containing $\hat{\boldsymbol{k}}$ and the background magnetic field. The gray dots in Figure 3d show that all cases have $\Delta V_1 > 0$, so the precursors mostly propagate away from their corresponding FT shocks. The relative velocities between the FT shock fronts and the precursor-wave fronts are also analyzed by calculating $\Delta V_2 = v_{\rm ph}^{\rm prf}\cos\theta_{\rm kn} - v_{\rm sh}^{\rm prf}$. Here $v_{\rm sh}^{\rm prf}$ is the FT shock velocity in the upstream SW plasma frame and a finite precursor-wave front size has been assumed. As shown by the diamonds in Figure 3d, 11 precursor cases have upstream-directed phase velocities ($\Delta V_2 > 0$), and 11 have downstream-directed phase velocities ($\Delta V_2 < 0$) with respect to their corresponding FT shocks.

5. Discussions

The precursor-wave properties and the relationship between the PWs and their corresponding FT shock parameters presented above can help to understand the possible precursor-wave generation mechanisms. At least three possible mechanisms have been proposed for the generation of lower hybrid frequency whistler precursors upstream of collisionless shocks, which are dispersive radiation (Kennel et al., 1985), slow-drift modified two-stream instability (MTSI) (e.g., Muschietti & Lembège, 2017), and fast-drift MTSI (Hull et al., 2020).

Whistler precursors may be an essential part of a collisionless shock, with the dispersive shock serving as the source of the waves (Dimmock et al., 2019; Kennel et al., 1985; Krasnoselskikh et al., 2002; Sundkvist et al., 2012). The transition of a dispersive shock with a periodic oscillating electric current drives waves at different frequencies, including whistler precursors (Tidman & Northrop, 1968). The precursors propagate parallel or oblique to the shock normal and with group velocities in the upstream direction (Mellott & Greenstadt, 1984; Tidman & Northrop, 1968; Wilson et al., 2017), carrying energy away from the shock ramp to balance the nonlinear shock steepening process (Sundkvist et al., 2012). The whistler precursors usually have large amplitudes comparable to the shock ramp amplitudes, and the shock ramp can be considered as the last and largest amplitude cycle in a whistler-precursor train (Wilson, 2016). For subcritical shocks, whistler precursors are expected to be radiated from the shock ramps for nearly all shock normal angles (Kennel et al., 1985). For supercritical shocks, whistler precursors are expected to stand upstream of quasi-perpendicular shocks (e.g., Balikhin et al., 1997; Krasnoselskikh et al., 1991; Oka et al., 2019). For supercritical quasi-parallel shocks, whistler precursors can be radiated dispersively from the ramp when a shock reformation cycle is completed (Scholer et al., 2003). In Figure 3a, the 8 quasi-parallel shocks and 14 out of the 21 quasi-perpendicular shocks analyzed have precursors. In addition, the whistler precursors have amplitudes comparable to the amplitudes of their corresponding FT shock ramps (Figure 3b), suggesting that they perhaps underwent nonlinear steepening (Yoon et al., 2014). The precursors propagate parallel or oblique to their corresponding FT shock normals with $\theta_{\rm kn}$ mostly smaller than 45° (Figure 3c). Similar features of whistler precursors upstream of interplanetary shocks were also reported (Wilson et al., 2017). More importantly, the PWs have upstream-directed group velocities and propagate away from the FT shocks (Figure 3d). These observed features are mostly consistent with the dispersive radiation mechanism (Kennel et al., 1985; Krasnoselskikh et al., 2002).

For supercritical quasi-perpendicular shocks, the slow-drift MTSI, an instability driven by the unmagnetized incoming SW ions and the magnetized electrons in the foot, can generate whistlers at quasi-perpendicular

propagation and with wavelengths of several λ_e (Gary et al., 1987; Muschietti & Lembège, 2017). The precursors observed upstream of the FT shocks propagate oblique to the background magnetic field ($5° < \theta_{kB} < 80°$ in Figure 2b) and have wavelengths on the order of λ_i (Figure 2d), inconsistent with the slow-drift MTSI. In addition, whistler precursors are suggested to arise through the fast-drift MTSI driven by the relative drift between the unmagnetized reflected ions and the magnetized electrons in the foot (Hull et al., 2020). The resultant whistler precursors are expected to have phase velocities pointing upstream as they need to Landau resonate with the reflected ions from the shocks (Gary et al., 1987; Wu et al., 1983). The ΔV_2 results of the wave phase velocities in Figure 3d do not support the fast-drift MTSI generation mechanism. Furthermore, for all FT shocks with precursors, the upstream electron beta is found to be larger than 0.5. This value is likely too large to allow the fast-drift MTSI to grow (Gary et al., 1987; Wu et al., 1983).

6. Conclusions

In this study, we perform the first statistical survey of the PWs upstream of FT shocks observed by MMS. The frequencies and wavenumbers of the PWs in the PRF are around the lower hybrid frequency and the ion inertial length, respectively. They are found to follow the cold plasma whistler-wave dispersion relation. Together with the feature of the right-hand polarization of the PWs in the PRF, they are identified as whistler-mode waves. In addition, the FT shocks have a wide range of θ_{Bn} of 20°–90° and moderate M_A of 2–7 compared with interplanetary shocks and planetary bow shocks. The statistical results show that the occurrence of whistler precursors upstream of the FT shocks is insensitive to their M_A and θ_{Bn}. Interestingly, in the FT shock frame, most of the precursors have group velocities pointing upstream, have large amplitudes, and propagate with $\theta_{kn} < 45°$. These observational features suggest that the precursors are likely generated through the dispersive radiation mechanism.

Data Availability Statement

The Space Physics Data Facility was used for access to ion data from MMS 1 (Gershman et al., 2022a), electron data from MMS 1 (Gershman et al., 2022b), FGM data from MMS 1 (Russell et al., 2022) and SCM data from four MMS spacecraft (Le Contel et al., 2022a, 2022b, 2022c, 2022d), respectively.

Acknowledgments
This research was funded by the National Natural Science Foundation of China (Grants 42225405, 42275135). We thank the MMS instrument teams and the MMS Science Data Center for providing the data. Mengmeng Wang thanks Dr. Jinxing Li for helpful discussions.

References

An, X., Liu, T. Z., Bortnik, J., Osmane, A., & Angelopoulos, V. (2020). Formation of foreshock transients and associated secondary shocks. *The Astrophysical Journal*, *901*(1), 73. https://doi.org/10.3847/1538-4357/abaf03

Balikhin, M. A., De Dudok Wit, T., Alleyne, H. S. C. K., Woolliscroft, L. J. C., Walker, S. N., Krasnosel'skikh, V., et al. (1997). Experimental determination of the dispersion of waves observed upstream of a quasi-perpendicular shock. *Geophysical Research Letters*, *24*(7), 787–790. https://doi.org/10.1029/97GL00671

Balogh, A., & Treumann, R. A. (2013). *Physics of collisionless shocks: Space plasma shock waves*. Springer. https://doi.org/10.1007/978-1-4614-6099-2

Brain, D. A., Bagenal, F., Acuña, M. H., Connerney, J. E. P., Crider, D. H., Mazelle, C., et al. (2002). Observations of low-frequency electromagnetic plasma waves upstream from the Martian shock. *Journal of Geophysical Research*, *107*(A6), SMP9-1–SMP9-11. https://doi.org/10.1029/2000JA000416

Burch, J. L., Moore, T. E., Torbert, R. B., & Giles, B. L. (2016). Magnetospheric multiscale overview and science objectives. *Space Science Reviews*, *199*(1–4), 5–21. https://doi.org/10.1007/s11214-015-0164-9

Davis, L. A., Cattell, C. A., Wilson, L. B., Cohen, Z. A., Breneman, A. W., & Hanson, E. L. M. (2021). ARTEMIS observations of plasma waves in laminar and perturbed interplanetary shocks. *The Astrophysical Journal*, *913*(2), 144. https://doi.org/10.3847/1538-4357/abf56a

Dimmock, A. P., Russell, C. T., Sagdeev, R. Z., Krasnoselskikh, V., Walker, S. N., Carr, C., et al. (2019). Direct evidence of nonstationary collisionless shocks in space plasmas. *Science Advances*, *5*(2), eaau9926. https://doi.org/10.1126/sciadv.aau9926

Eastwood, J. P., Balogh, A., Lucek, E. A., Mazelle, C., & Dandouras, I. (2005). Quasi-monochromatic ULF foreshock waves as observed by the four-spacecraft Cluster mission: 1. Statistical properties. *Journal of Geophysical Research*, *110*(A11), A11219. https://doi.org/10.1029/2004JA010617

Eastwood, J. P., Lucek, E. A., Mazelle, C., Meziane, K., Narita, Y., Pickett, J., & Treumann, R. A. (2005). The foreshock. *Space Science Reviews*, *118*(1–4), 41–94. https://doi.org/10.1007/s11214-005-3824-3

Fairfield, D. H. (1974). Whistler waves observed upstream from collisionless shocks. *Journal of Geophysical Research*, *79*(10), 1368–1378. https://doi.org/10.1029/ja079i010p01368

Fairfield, D. H., & Behannon, K. W. (1976). Bow shock and magnetosheath waves at Mercury. *Journal of Geophysical Research*, *81*(22), 3897–3906. https://doi.org/10.1029/JA081i022p03897

Gary, S. P., Tokar, R. L., & Winske, D. (1987). Ion/ion and electron/ion cross-field instabilities near the lower hybrid frequency. *Journal of Geophysical Research*, *92*(A9), 10029–10038. https://doi.org/10.1029/ja092ia09p10029

Gershman, D. J., Giles, B. L., Pollock, C. J., Moore, T. E., & Burch, J. L. (2022a). MMS 1 fast plasma investigation, dual ion spectrometer (FPI, DIS) distribution moments, level 2 (L2), burst mode, 0.15 s data [Dataset]. *NASA Space Physics Data Facility*. https://doi.org/10.48322/qggf-vr83

Gershman, D. J., Giles, B. L., Pollock, C. J., Moore, T. E., & Burch, J. L. (2022b). MMS 1 fast plasma investigation, dual electron spectrometer (FPI, DES) distribution moments, level 2 (L2), burst mode, 30 ms data [Dataset]. *NASA Space Physics Data Facility*. https://doi.org/10.48322/6172-zw20

Halekas, J. S., Brain, D. A., Mitchell, D. L., & Lin, R. P. (2006). Whistler waves observed near lunar crustal magnetic sources. *Geophysical Research Letters*, *33*(22), L22104. https://doi.org/10.1029/2006GL027684

Harada, Y., & Halekas, J. S. (2016). Upstream waves and particles at the Moon. In *Low-frequency waves in space plasmas* (pp. 307–322). https://doi.org/10.1002/9781119055006.ch18

Hull, A. J., Muschietti, L., Le Contel, O., Dorelli, J. C., & Lindqvist, P. A. (2020). MMS observations of intense whistler waves within Earth's supercritical bow shock: Source mechanism and impact on shock structure and plasma transport. *Journal of Geophysical Research: Space Physics*, *125*(7), e2019JA027290. https://doi.org/10.1029/2019JA027290

Hull, A. J., Muschietti, L., Oka, M., Larson, D. E., Mozer, F. S., Chaston, C. C., et al. (2012). Multiscale whistler waves within Earth's perpendicular bow shock. *Journal of Geophysical Research*, *117*(A12), A12104. https://doi.org/10.1029/2012JA017870

Kennel, C. F., Edmiston, J. P., & Hada, T. (1985). A quarter century of collisionless shock research (pp. 1–36). https://doi.org/10.1029/GM034p0001

Krasnoselskikh, V., Balikhin, M., Walker, S. N., Schwartz, S., Sundkvist, D., Lobzin, V., et al. (2013). The dynamic quasiperpendicular shock: Cluster discoveries. *Space Science Reviews*, *178*(2–4), 535–598. https://doi.org/10.1007/s11214-013-9972-y

Krasnoselskikh, V. V., Balikhin, M. A., Alleyne, H. S. C., Klimov, S. I., Mier-Jedrzejowicz, W. A. C., Pardaens, A. K., et al. (1991). On the nature of low frequency turbulence in the foot of strong quasi-perpendicular shocks. *Advances in Space Research*, *11*(9), 15–18. https://doi.org/10.1016/0273-1177(91)90002-2

Krasnoselskikh, V. V., Lembège, B., Savoini, P., & Lobzin, V. V. (2002). Nonstationarity of strong collisionless quasiperpendicular shocks: Theory and full particle numerical simulations. *Physics of Plasmas*, *9*(4), 1192–1209. https://doi.org/10.1063/1.1457465

Lalti, A., Khotyaintsev, Y. V., Graham, D. B., Vaivads, A., Steinvall, K., & Russell, C. T. (2022). Whistler waves in the foot of quasi-perpendicular supercritical shocks. *Journal of Geophysical Research: Space Physics*, *127*(5), e2021JA029969. https://doi.org/10.1029/2021JA029969

Le Contel, O., Leroy, P., Roux, A., Coillot, C., Alison, D., Bouabdellah, A., et al. (2016). The search-coil magnetometer for MMS. *Space Science Reviews*, *199*(1–4), 257–282. https://doi.org/10.1007/s11214-014-0096-9

Le Contel, O., Torbert, R. B., Mirioni, L., Argall, M. R., & Burch, J. L. (2022a). MMS 1 search coil magnetometer (SCM) AC magnetic field level 2 (L2), burst mode, 8192 sample/s data [Dataset]. *NASA Space Physics Data Facility*. https://doi.org/10.48322/gyvg-pf49

Le Contel, O., Torbert, R. B., Mirioni, L., Argall, M. R., & Burch, J. L. (2022b). MMS 2 search coil magnetometer (SCM) AC magnetic field level 2 (L2), burst mode, 8192 sample/s data [Dataset]. *NASA Space Physics Data Facility*. https://doi.org/10.48322/axbs-qh32

Le Contel, O., Torbert, R. B., Mirioni, L., Argall, M. R., & Burch, J. L. (2022c). MMS 3 search coil magnetometer (SCM) AC magnetic field level 2 (L2), burst mode, 8192 sample/s data [Dataset]. *NASA Space Physics Data Facility*. https://doi.org/10.48322/mg2d-6848

Le Contel, O., Torbert, R. B., Mirioni, L., Argall, M. R., & Burch, J. L. (2022d). MMS 4 search coil magnetometer (SCM) AC magnetic field level 2 (L2), burst mode, 8192 sample/s data [Dataset]. *NASA Space Physics Data Facility*. https://doi.org/10.48322/kp2d-gb32

Lin, Y. (1997). Generation of anomalous flows near the bow shock by its interaction with interplanetary discontinuities. *Journal of Geophysical Research*, *102*(A11), 24265–24281. https://doi.org/10.1029/97JA01989

Liu, T. Z., An, X., Zhang, H., & Turner, D. (2020). Magnetospheric multiscale observations of foreshock transients at their very early stage. *The Astrophysical Journal*, *902*(1), 5. https://doi.org/10.3847/1538-4357/abb249

Liu, T. Z., Hietala, H., Angelopoulos, V., & Turner, D. L. (2016). Observations of a new foreshock region upstream of a foreshock bubble's shock. *Geophysical Research Letters*, *43*(10), 4708–4715. https://doi.org/10.1002/2016GL068984

Liu, Z. Y., Wang, B., Zong, Q. G., Yao, S. T., Pollock, C. J., & Le, G. (2021). Thermal electron behavior in obliquely propagating whistler waves: MMS observations in the solar wind. *Geophysical Research Letters*, *48*(14), e2021GL094099. https://doi.org/10.1029/2021GL094099

Matsukiyo, S., & Scholer, M. (2006). On microinstabilities in the foot of high Mach number perpendicular shocks. *Journal of Geophysical Research*, *111*(6), A06104. https://doi.org/10.1029/2005JA011409

Mazelle, C., Lembège, B., Morgenthaler, A., Meziane, K., Horbury, T. S., Génot, V., et al. (2010). Self-reformation of the quasi-perpendicular shock: CLUSTER observations. In *AIP conference proceedings* (Vol. 1216, pp. 471–474). https://doi.org/10.1063/1.3395905

Mellott, M. M., & Greenstadt, E. W. (1984). The structure of oblique subcritical bow shocks: ISEE 1 and 2 observations. *Journal of Geophysical Research*, *89*(A4), 2151–2161. https://doi.org/10.1029/JA089iA04p02151

Muschietti, L., & Lembège, B. (2017). Two-stream instabilities from the lower-hybrid frequency to the electron cyclotron frequency: Application to the front of quasi-perpendicular shocks. *Annales Geophysicae*, *35*(5), 1093–1112. https://doi.org/10.5194/angeo-35-1093-2017

Oka, M., Otsuka, F., Matsukiyo, S., Wilson, L. B., Argall, M. R., Amano, T., et al. (2019). Electron scattering by low-frequency whistler waves at Earth's bow shock. *The Astrophysical Journal*, *886*(1), 53. https://doi.org/10.3847/1538-4357/ab4a81

Omidi, N., Eastwood, J. P., & Sibeck, D. G. (2010). Foreshock bubbles and their global magnetospheric impacts. *Journal of Geophysical Research*, *115*(A6), A06204. https://doi.org/10.1029/2009JA014828

Orlowski, D. S., & Russell, C. T. (1991). Ulf waves upstream of the Venus bow shock: Properties of one-hertz waves. *Journal of Geophysical Research*, *96*(A7), 11271–11282. https://doi.org/10.1029/91JA01103

Orlowski, D. S., Russell, C. T., & Lepping, R. P. (1992). Wave phenomena in the upstream region of Saturn. *Journal of Geophysical Research*, *97*(A12), 19187–19199. https://doi.org/10.1029/92JA01461

Pollock, C., Moore, T., Jacques, A., Burch, J., Gliese, U., Saito, Y., et al. (2016). Fast plasma investigation for magnetospheric multiscale. *Space Science Reviews*, *199*(1–4), 331–406. https://doi.org/10.1007/s11214-016-0245-4

Russell, C. T. (2007). Upstream whistler-mode waves at planetary bow shocks: A brief review. *Journal of Atmospheric and Solar-Terrestrial Physics*, *69*(14), 1739–1746. https://doi.org/10.1016/j.jastp.2006.11.004

Russell, C. T., Anderson, B. J., Baumjohann, W., Bromund, K. R., Dearborn, D., Fischer, D., et al. (2016). The magnetospheric multiscale magnetometers. *Space Science Reviews*, *199*(1–4), 189–256. https://doi.org/10.1007/s11214-014-0057-3

Russell, C. T., Magnes, W., Wei, H., Bromund, K. R., Plaschke, F., Fischer, D., et al. (2022). MMS 1 flux gate magnetometer (FGM) DC magnetic field, level 2 (L2), burst mode, 128 sample/s, v4/5 data [Dataset]. *NASA Space Physics Data Facility*. https://doi.org/10.48322/pj0n-m695

Santolík, O., Parrot, M., & Lefeuvre, F. (2003). Singular value decomposition methods for wave propagation analysis. *Radio Science*, *38*(1). https://doi.org/10.1029/2000RS002523

Scholer, M., & Burgess, D. (2007). Whistler waves, core ion heating, and nonstationarity in oblique collisionless shocks. *Physics of Plasmas*, *14*(7), 072103. https://doi.org/10.1063/1.2748391

Scholer, M., Kucharek, H., & Shinohara, I. (2003). Short large-amplitude magnetic structures and whistler wave precursors in a full-particle quasi-parallel shock simulation. *Journal of Geophysical Research*, *108*(A7), 1273. https://doi.org/10.1029/2002JA009820

Schwartz, S. J. (1998). Analysis methods for multi-spacecraft data. In P. Gotz, & P. W. Daly (Eds.), *ISSI scientific reports series* (p. 249).
Schwartz, S. J., Chaloner, C. P., Christiansen, P. J., Coates, A. J., Hall, D. S., Johnstone, A. D., et al. (1985). An active current sheet in the solar wind. *Nature*, *318*(6043), 269–271. https://doi.org/10.1038/318269a0
Scudder, J. D., Mangeney, A., Lacombe, C., Harvey, C. C., Wu, C. S., & Anderson, R. R. (1986). The resolved layer of a collisionless, high β, supercritical, quasi-perpendicular shock wave: 3. Vlasov electrodynamics. *Journal of Geophysical Research*, *91*(A10), 11075–11097. https://doi.org/10.1029/ja091ia10p11075
Shi, Q. Q., Tian, A. M., Bai, S. C., Hasegawa, H., Degeling, A. W., Pu, Z. Y., et al. (2019). Dimensionality, coordinate system and reference frame for analysis of in-situ space plasma and field data. *Space Science Reviews*, *215*(4), 35. https://doi.org/10.1007/s11214-019-0601-2
Smith, C. W., Wong, H. K., & Goldstein, M. L. (1991). Whistler waves associated with the Uranian bow shock: Outbound observations. *Journal of Geophysical Research*, *96*(A9), 15841–15852. https://doi.org/10.1029/91JA01460
Sonnerup, B., & Scheible, M. (1998). Minimum and maximum variance analysis. In G. Paschmann, & P. W. Daly (Eds.), *Analysis methods for multi-spacecraft data* (Vol. 001, pp. 185–220).
Stringer, T. E. (1963). Low-frequency waves in an unbounded plasma. *Journal of Nuclear Energy Part C: Plasma Physics, Accelerators, Thermonuclear Research*, *5*(2), 89–107. https://doi.org/10.1088/0368-3281/5/2/304
Sulaiman, A. H., Gurnett, D. A., Halekas, J. S., Yates, J. N., Kurth, W. S., & Dougherty, M. K. (2017). Whistler mode waves upstream of Saturn. *Journal of Geophysical Research: Space Physics*, *122*(1), 227–234. https://doi.org/10.1002/2016JA023501
Sundkvist, D., Krasnoselskikh, V., Bale, S. D., Schwartz, S. J., Soucek, J., & Mozer, F. (2012). Dispersive nature of high Mach number collisionless plasma shocks: Poynting flux of oblique whistler waves. *Physical Review Letters*, *108*(2), 025002. https://doi.org/10.1103/PhysRevLett.108.025002
Tidman, D. A., & Northrop, T. G. (1968). Emission of plasma waves by the Earth's bow shock. *Journal of Geophysical Research*, *73*(5), 1543–1553. https://doi.org/10.1029/ja073i005p01543
Turner, D. L., Liu, T. Z., Wilson, L. B., Cohen, I. J., Gershman, D. G., Fennell, J. F., et al. (2020). Microscopic, multipoint characterization of foreshock bubbles with magnetospheric multiscale (MMS). *Journal of Geophysical Research: Space Physics*, *125*(7), e2019JA027707. https://doi.org/10.1029/2019JA027707
Turner, D. L., Omidi, N., Sibeck, D. G., & Angelopoulos, V. (2013). First observations of foreshock bubbles upstream of Earth's bow shock: Characteristics and comparisons to HFAs. *Journal of Geophysical Research: Space Physics*, *118*(4), 1552–1570. https://doi.org/10.1002/jgra.50198
Turner, D. L., Wilson, L. B., Goodrich, K. A., Madanian, H., Schwartz, S. J., Liu, T. Z., et al. (2021). Direct multipoint observations capturing the reformation of a supercritical fast magnetosonic shock. *The Astrophysical Journal Letters*, *911*(2), L31. https://doi.org/10.3847/2041-8213/abec78
Verkhoglyadova, O. P., Tsurutani, B. T., & Lakhina, G. S. (2010). Properties of obliquely propagating chorus. *Journal of Geophysical Research*, *115*(A9), A00F19. https://doi.org/10.1029/2009JA014809
Vu, A., Liu, T. Z., Zhang, H., & Pollock, C. (2022). Statistical study of foreshock bubbles, hot flow anomalies, and spontaneous hot flow anomalies and their substructures observed by MMS. *Journal of Geophysical Research: Space Physics*, *127*(2), e2021JA030029. https://doi.org/10.1029/2021JA030029
Wang, S., Chen, L., Ng, J., Bessho, N., Le, G., Fung, S. F., et al. (2020). A case study of nonresonant mode 3-s ULF waves observed by MMS. *Journal of Geophysical Research: Space Physics*, *125*(11), e2020JA028557. https://doi.org/10.1029/2020JA028557
Wang, Y., Zhong, J., Slavin, J., Zhang, H., Lee, L., Shan, L., et al. (2023). MESSENGER observations of standing whistler waves upstream of Mercury's bow shock. *Geophysical Research Letters*, *50*(10), e2022GL102574. https://doi.org/10.1029/2022GL102574
Wilson, L. B. (2016). Low frequency waves at and upstream of collisionless shocks. In *Low-frequency waves in space plasmas* (pp. 269–291). https://doi.org/10.1002/9781119055006.ch16
Wilson, L. B., Brosius, A. L., Gopalswamy, N., Nieves-Chinchilla, T., Szabo, A., Hurley, K., et al. (2021). A quarter century of wind spacecraft discoveries. *Reviews of Geophysics*, *59*(2), e2020RG000714. https://doi.org/10.1029/2020RG000714
Wilson, L. B., Goodrich, K. A., Turner, D. L., Cohen, I. J., Whittlesey, P. L., & Schwartz, S. J. (2022). The need for accurate measurements of thermal velocity distribution functions in the solar wind. *Frontiers in Astronomy and Space Sciences*, *9*, 1–15. https://doi.org/10.3389/fspas.2022.1063841
Wilson, L. B., Koval, A., Szabo, A., Breneman, A., Cattell, C. A., Goetz, K., et al. (2012). Observations of electromagnetic whistler precursors at supercritical interplanetary shocks. *Geophysical Research Letters*, *39*(8), L08109. https://doi.org/10.1029/2012GL051581
Wilson, L. B., Koval, A., Szabo, A., Stevens, M. L., Kasper, J. C., Cattell, C. A., & Krasnoselskikh, V. V. (2017). Revisiting the structure of low-Mach number, low-beta, quasi-perpendicular shocks. *Journal of Geophysical Research: Space Physics*, *122*(9), 9115–9133. https://doi.org/10.1002/2017JA024352
Wilson, L. B., Sibeck, D. G., Breneman, A. W., Le Contel, O., Cully, C., Turner, D. L., et al. (2014). Quantified energy dissipation rates in the terrestrial bow shock: 1. Analysis techniques and methodology. *Journal of Geophysical Research: Space Physics*, *119*(8), 6455–6474. https://doi.org/10.1002/2014JA019929
Wu, C. S., Zhou, Y. M., Tsai, S. T., Guo, S. C., Winske, D., & Papadopoulos, K. (1983). A kinetic cross-field streaming instability. *Physics of Fluids*, *26*(5), 1259–1267. https://doi.org/10.1063/1.864285
Yao, S. T., Shi, Q. Q., Zong, Q. G., Degeling, A. W., Guo, R. L., Li, L., et al. (2021). Low-frequency whistler waves modulate electrons and generate higher-frequency whistler waves in the solar wind. *The Astrophysical Journal*, *923*(2), 216. https://doi.org/10.3847/1538-4357/ac2e97
Yoon, P. H., Pandey, V. S., & Lee, D.-H. (2014). Oblique nonlinear whistler wave. *Journal of Geophysical Research: Space Physics*, *119*(3), 1851–1862. https://doi.org/10.1002/2013JA018993
Zhang, H., Zong, Q., Connor, H., Delamere, P., Facskó, G., Han, D., et al. (2022). Dayside transient phenomena and their impact on the magnetosphere and ionosphere. *Space Science Reviews*, *218*(5), 40. https://doi.org/10.1007/s11214-021-00865-0